Numerical Analysis of Three-Dimensional Viscous Internal Flows

Rodrick V. Chima*
NASA Lewis Research Center, Cleveland, Ohio 44135
and
Jeffrey W. Yokota*
Sverdrup Technology, Inc., Cleveland, Ohio 44130

A three-dimensional Navier-Stokes code has been developed for analysis of turbomachinery blade rows and other internal flows. The Navier-Stokes equations are written in a Cartesian coordinate system rotating about the x axis, then mapped to a general body-fitted coordinate system. Streamwise viscous terms are neglected and turbulence effects are modeled using the Baldwin–Lomax model. A finite-difference discretization is used on stacked C-type grids. The equations are solved using a multistage Runge-Kutta algorithm with a spatially varying time step and implicit residual smoothing. Calculations were made of a horseshoe vortex formed in front of a blunt flat plate standing in a turbulent endwall boundary layer. Comparisons are made with experimental data for a circular cylinder under similar conditions. Calculated details of the primary vortex show good agreement with the experimental data. The calculations also show a small secondary vortex that was not seen experimentally. Calculations were also made of a subsonic annular turbine stator and compared to experimental data. Computed surface pressure distributions compare well with measured values at three spanwise locations. The endwall boundary layers produce horseshoe vortices at the leading edge of the blade. Computed wake profiles resemble the measured profiles, but computed efficiencies are lower than that of measured values by a factor of two.

Introduction

MUCH of our work in the past few years has involved the analysis of two-dimensional or quasi-three-dimensional blade-to-blade flows in turbomachinery.[1,2] In Refs. 1 and 2, both Euler and Navier-Stokes results were presented for each blade row considered, and in each case a significant viscous effect was observed. These effects include such things as a pressure-surface or "cove" separation on an axial turbine blade, a reduction in the choking mass flow and a change in shock location for an axial compressor blade, and a reduction in the peak Mach number and shock strength near the leading edge of a centrifugal impeller. Each of these two-dimensional viscous effects can be expected to lead to secondary flows in three dimensions. Complex geometries, endwall boundary layers, tip-clearance effects, etc., also lead to three-dimensional flows in turbomachinery. It is the goal of the present work to begin to predict some of these three-dimensional viscous effects.

Several steady three-dimensional analyses for turbomachinery have been published lately. Among them are the work of Dawes[3] and Subramanian and Bozzola.[4] Both used Runge-Kutta schemes implemented on sheared H-type grids. H-grids are particularly easy to generate and implement for turbomachinery calculations, but suffer from poor leading-edge resolution. Rai[5] has published a notable analysis of unsteady three-dimensional rotor-stator interaction in an axial turbine. He used a third-order-accurate upwind implicit scheme and a system of patched and overlaid O- and H-type grids for good

resolution of viscous phenomena. His analysis has not been used for steady flows, however.

In this paper, we describe a numerical method for analyzing three-dimensional viscous flows in isolated turbomachinery blade passages. The underlying Cartesian formulation allows the method to be applied easily to both Cartesian and cylindrical geometries. Stacked C-type grids give good resolution of critical leading-edge regions.

A multistage Runge-Kutta scheme is used to solve the finite-difference form of the thin-layer Navier-Stokes equations with a Baldwin-Lomax turbulence model. A spatially varying time step and implicit residual smoothing are used to accelerate convergence of the scheme to a steady state. Two calculations are presented to validate the analysis. The first calculation shows the formation of a horseshoe vortex at the leading edge of a flat plate with a round leading edge that stands in a turbulent endwall boundary layer. Comparisons made between calculated results and experimental data for a circular cylinder under similar conditions show good agreement between static pressure distributions and flow visualization pictures on the endwall, and between static and total pressure contours and velocity vector plots made on the symmetry plane. The second calculation is of the flow through an annular turbine stator. Comparisons made between calculated and measured static pressure distributions compare well at three spanwise locations.

Governing Equations

The Navier-Stokes equations are written in a Cartesian (x,y,z) coordinate system rotating with angular velocity Ω about the x axis. The rotation introduces source terms in the y- and z-momentum equations. The Cartesian equations are mapped to a general body-fitted (ξ,η,ζ) coordinate system using standard techniques. The ξ-coordinate direction is assumed to follow the flow direction, and the thin-layer approximation is used to drop all viscous derivatives in this direction. All viscous terms in the cross-channel (η,ζ) plane are retained,

with an option in the code to delete all cross derivatives if desired. The resulting equations are as follows:

$$\partial_t q + J[\partial_\xi \hat{E} + \partial_\eta \hat{F} + \partial_\zeta \hat{G} - Re^{-1}(\partial_\eta \hat{F}_V + \partial_\zeta \hat{G}_V)] = H \quad (1)$$

where

$$\hat{q} = J^{-1} \begin{bmatrix} \rho \\ \rho u \\ \rho v \\ \rho w \\ e \end{bmatrix}, \quad H = \begin{bmatrix} 0 \\ 0 \\ -\Omega \rho w \\ \Omega \rho v \\ 0 \end{bmatrix},$$

$$\hat{E} = J^{-1} \begin{bmatrix} \rho U' \\ \rho u U' + \xi_x p \\ \rho v U' + \xi_y p \\ \rho w U' + \xi_z p \\ e U' + p U \end{bmatrix}, \quad \hat{F} = J^{-1} \begin{bmatrix} \rho V' \\ \rho u V' + \eta_x p \\ \rho v V' + \eta_y p \\ \rho w V' + \eta_z p \\ e V' + p V \end{bmatrix},$$

$$\hat{G} = J^{-1} \begin{bmatrix} \rho W' \\ \rho u W' + \zeta_x p \\ \rho v W' + \zeta_y p \\ \rho w W' + \zeta_z p \\ e W' + p W \end{bmatrix}$$

$$(2)$$

These equations are written in a coordinate system that rotates with the blade. Velocities u, v, and w are defined with respect to the absolute or laboratory frame of reference. Relative velocities (denoted by a prime) are found by subtracting the wheel speed from the absolute velocity, giving

$$u' = u \quad (3a)$$

$$v' = v - \Omega z \quad (3b)$$

$$w' = w + \Omega y \quad (3c)$$

The relative contravariant velocity components are given by

$$U' = \xi_x u + \xi_y v' + \xi_z w' \quad (4a)$$

$$V' = \eta_x u + \eta_y v' + \eta_z w' \quad (4b)$$

$$W' = \zeta_x u + \zeta_y v' + \zeta_z w' \quad (4c)$$

Note that although $u' = u$, $U' \neq U$.

The energy and static pressure are given by

$$e = \rho[C_v T + (u^2 + v^2 + w^2)/2] \quad (5)$$

$$p = (\gamma - 1)[e - \rho(u^2 + v^2 + w^2)/2] \quad (6)$$

Using Stokes' hypothesis, $\lambda = -\frac{2}{3}\mu$, the viscous flux $\hat{F}_V$ can be written as follows:

$$\hat{F}_V = J^{-1}\mu[0, F_2, F_3, F_4, F_5]^T \quad (7a)$$

where

$$F_2 = C_1\partial_\eta u + C_2\eta_x + C_3\partial_\zeta u - C_4\eta_x + C_5\zeta_x$$

$$F_3 = C_1\partial_\eta v + C_2\eta_y + C_3\partial_\zeta v - C_4\eta_y + C_5\zeta_y$$

$$F_4 = C_1\partial_\eta w + C_2\eta_z + C_3\partial_\zeta w - C_4\eta_z + C_5\zeta_z$$

$$F_5 = \mu\gamma/Pr\,[C_1\partial_\eta(C_v T) + C_3\partial_\zeta(C_v T)] + uF_2 + vF_3 + wF_4$$

$$(7b)$$

and

$$C_1 = \eta_x^2 + \eta_y^2 + \eta_z^2$$

$$C_2 = \frac{1}{3}(\eta_x\partial_\eta u + \eta_y\partial_\eta v + \eta_z\partial_\eta w)$$

$$C_3 = \eta_x\zeta_x + \eta_y\zeta_y + \eta_z\zeta_z$$

$$C_4 = \frac{2}{3}(\zeta_x\partial_\zeta u + \zeta_y\partial_\zeta v + \zeta_z\partial_\zeta w)$$

$$C_5 = \eta_x\partial_\zeta u + \eta_y\partial_\zeta v + \eta_z\partial_\zeta w \quad (7c)$$

Terms multiplied by C_1 and C_2 lead to nonmixed second-derivative viscous terms such as $u_{\eta\eta}$, whereas terms multiplied by C_3-C_5 lead to mixed-derivative terms such as $u_{\eta\zeta}$. The viscous flux vector $\hat{G}$ can be written similarly, with directions η and ζ everywhere interchanged.

Metric terms are defined using the following relations.

$$\begin{bmatrix} \xi_x & \eta_x & \zeta_x \\ \xi_y & \eta_y & \zeta_y \\ \xi_z & \eta_z & \zeta_z \end{bmatrix} = J \begin{bmatrix} y_\eta z_\zeta - y_\zeta z_\eta & y_\zeta z_\xi - y_\xi z_\zeta & y_\xi z_\eta - y_\eta z_\xi \\ x_\zeta z_\eta - x_\eta z_\zeta & x_\xi z_\zeta - x_\zeta z_\xi & x_\eta z_\xi - x_\xi z_\eta \\ x_\eta y_\zeta - x_\zeta y_\eta & x_\zeta y_\xi - x_\xi y_\zeta & x_\xi y_\eta - x_\eta y_\xi \end{bmatrix}$$

$$(8)$$

where

$$J = (x_\xi y_\eta z_\zeta + x_\zeta y_\xi z_\eta + x_\eta y_\zeta z_\xi - x_\xi y_\zeta z_\eta - x_\eta y_\xi z_\zeta - x_\zeta y_\eta z_\xi)^{-1}$$

$$(9)$$

The equations are nondimensionalized by arbitrary reference quantities (here the inlet total density ρ_{0ref} and the total sonic velocity c_{0ref} were used), and the Reynolds number Re and Prandtl number Pr are defined in terms of these quantities. The equations assume that the specific heats C_p and C_v and Prandtl number are constant, that Stoke's hypothesis is valid, and that the effective viscosity for turbulent flows may be written as

$$\mu_{\text{eff}} = \mu_{\text{lam}} + \mu_{\text{turb}} \quad (10)$$

where the laminar viscosity is calculated using a power-law function of temperature:

$$\frac{\mu_{\text{lam}}}{\mu_{\text{ref}}} = \left(\frac{T}{T_{\text{ref}}}\right)^n \quad (11)$$

with $n = \frac{2}{3}$ for air.

Turbulence Model

The Baldwin-Lomax turbulence model[6] is applied on cross-channel (η,ζ) planes. Briefly, this is an algebraic two-layer eddy viscosity model based on the Cebeci-Smith method with modifications made to avoid having to locate the edge of the boundary layer. A Prandtl-VanDriest formulation is used in the inner region, and a Clauser formulation with a Klebanoff intermittency function is used in the outer region. The Baldwin-Lomax model is normally applied along a grid line crossing a single boundary layer. Two modifications to the model were made to account for the two boundary layers where the blade and endwall intersect.

First, the distance from the wall is calculated using the Buleev[7] length scale d:

$$d = \frac{2s_\eta s_\zeta}{s_\eta + s_\zeta + (s_\eta^2 + s_\zeta^2)^{1/2}} \quad (12)$$

where s_η and s_ζ are normal distances from the walls in the η and ζ directions, respectively. This length scale has the desirable property that d approaches the normal distance from one wall at large distances from the other wall.

Second, the turbulent viscosities are calculated across each
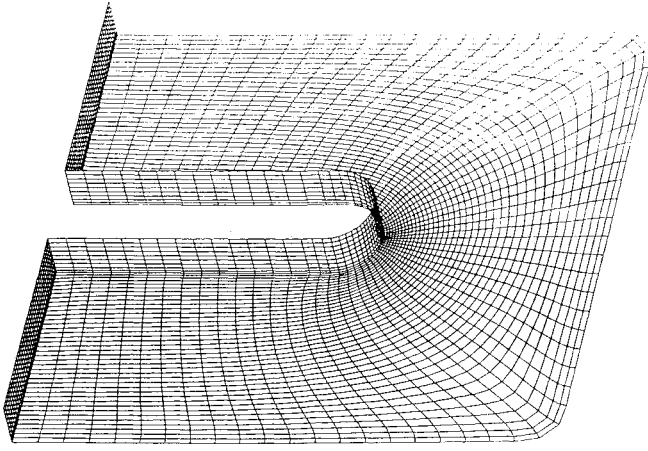
Eckerle & Langstons Horseshoe Vortex Experiment
Mach   0.196   Re   538257.   Alpha   0.00   Iter   4000

Fig. 1   Computational grid for the horseshoe vortex problem.

boundary layer or wake separately, then the total turbulent viscosity is taken as the vector sum of the components, i.e.,

$$\mu_{turb} = (\mu_{turb\eta}^2 + \mu_{turb\zeta}^2)^{1/2} \qquad (13)$$

This assumption has the desirable properties that outside of one viscous layer μ_{turb} takes on values calculated for the other layer, that it goes to zero in the core flow, and that near corners it accounts for both walls.

Computational Grid

Two-dimensional body-fitted grids for this work were generated using the GRAPE code developed by Sorenson.[8] Three-dimensional grids were formed by stacking the two-dimensional grids. Figure 1 shows a three-dimensional grid around a plate with a round leading edge. For annular geometries, the two-dimensional grids were stacked along a radial stacking line and stretched in the η direction so that the blade shape remained constant and the angular pitch of the outer (periodic) boundary remained constant.

Boundary Conditions

At the inlet, total temperature T_{0ref} is specified as a constant. A ζ distribution of total pressure (P_0/P_{0ref}) is specified as a constant or as appropriate for an inlet boundary layer with given thickness and a power-law velocity profile. For Cartesian geometries, the (x,y) and (x,z) flow angles are specified. For cylindrical geometries, the (x,y) flow angle is replaced by inlet whirl rv_θ.

For supersonic inlet flows, all flow variables are specified at the inlet. For subsonic flows, the inlet conditions are updated at each iteration by extrapolating the upstream-running Riemann invariant R^- based on the absolute total velocity $Q = \sqrt{u^2 + v^2 + w^2}$ to the inlet.

$$R^- = Q - \frac{2c}{\gamma - 1} \qquad (14)$$

The total velocity is then found from T_{0ref} using

$$Q = \frac{(\gamma - 1)R^- + \sqrt{2(1 - \gamma)(R^-)^2 + 4(\gamma + 1)C_p T_{0ref}}}{(\gamma + 1)} \qquad (15)$$

Velocity components are found from Q and the specified angles or whirl. Within the endwall boundary layer, that is, where $P_0/P_{0ref} < 1$, the v and w velocity components are found

by extrapolation from upstream. The density is found using

$$\frac{\rho}{\rho_{0ref}} = \frac{P_0}{P_{0ref}}\left[\frac{\gamma - 1}{2}\frac{(Q - R^-)}{c_{0ref}}\right]^{\frac{2}{\gamma - 1}} \qquad (16)$$

For subsonic outflow, the exit static pressure is specified and $(\rho, \rho u, \rho v, \rho w)$ are extrapolated. For Cartesian geometries the exit pressure is constant. For annular geometries, the hub pressure is specified and the radial pressure distribution is found by integrating the axisymmetric radial momentum equation:

$$\frac{dp}{dr} = \frac{\rho v_\theta^2}{r} = \frac{\rho}{r^3}(vz - wy)^2 \qquad (17)$$

Sidewalls and the trailing-edge cut are treated as periodic boundaries.

On the blade surface $V' = 0$, and for viscous flows $U' = W' = 0$. Blade surface pressures are found from the normal momentum equation. On the hub $(\zeta = 1)$ and tip $(\zeta = \zeta_{max})$,

$$(\zeta_x\xi_x + \zeta_y\xi_y + \zeta_z\xi_z)\partial_\xi p + (\zeta_x\eta_x + \zeta_y\eta_y + \zeta_z\eta_z)\partial_\eta p$$

$$+ (\zeta_x^2 + \zeta_y^2 + \zeta_z^2)\partial_\zeta p$$

$$= -\rho[\Omega(\zeta_y w - \zeta_z v) + U'(\zeta_x\partial_\xi u + \zeta_y\partial_\xi v + \zeta_z\partial_\xi w)$$

$$+ V'(\zeta_x\partial_\eta u + \zeta_y\partial_\eta v + \zeta_z\partial_\eta w)] \qquad (18)$$

On the blades $(\eta = 1)$, the normal momentum equation can be found from Eq. (18) by replacing ζ everywhere by η and V' by W'.

Multistage Runge-Kutta Algorithm

The governing equations are discretized using a node-centered finite-difference scheme. Second-order central differences are used throughout.

The multistage Runge-Kutta scheme developed by Jameson et al[9], is used to advance the flow equations in time from an initial guess to a steady state. If we rewrite Eq. (1) as

$$\partial_t q = -J[R_I - (R_V + D)] \qquad (19)$$

where R_I is the inviscid residual including the source term, R_V the viscous residual, and D an artificial dissipation term described in the next section, then the multistage Runge-Kutta algorithm can be written as follows:

$$q_0 = q_n$$

$$q_1 = q_0 - \alpha_1 J\Delta t[R_I q_0 - (R_V + D)q_0]$$

$$\vdots$$

$$q_k = q_0 - \alpha_k J\Delta t[R_I q_{k-1} - (R_V + D)q_0]$$

$$q_{n+1} = q_k \qquad (20)$$

For efficiency, both the physicial and artificial dissipation terms are calculated only at the first stage, then are held constant for subsequent stages.

Artificial Dissipation

The dissipative term D in Eq. (19) is a nonconservative version of that used by Jameson et al.[9] The lack of conservation is inconsequential for the subsonic results in this paper. However, we have had good success using this form of dissipation for supersonic cascades in two dimensions. The dissipa-

tive term is given by

$$Dq = (D_\xi + D_\eta + D_\zeta)q \qquad (21a)$$

where the ξ-direction operator is give by

$$D_\xi q = C(V_2 q_{\xi\xi} - V_4 q_{\xi\xi\xi\xi}) \qquad (21b)$$

and

$$C = \frac{1}{J\Delta t} \qquad (21c)$$

is a coefficient that makes the dissipation dimensionally consistent with the other fluxes. To minimize the artificial dissipation in viscous regions, we reduce C linearly across several grid points to zero at the walls.

The terms V_2 and V_4 are given by

$$V_2 = \mu_2 \max(\nu_{i+1}, \nu_i, \nu_{i-1})$$

$$V_4 = \max(0, \mu_4 - V_2) \qquad (21d)$$

where

$$\nu_{i,j} = \frac{|P_{i+1,j} - 2P_{i,j} + P_{i-1,j}|}{|P_{i+1,j} + 2P_{i,j} + P_{i-1,j}|} \qquad (21e)$$

and

$$\mu_2 = \mathcal{O}(1)$$

$$\mu_2 = \mathcal{O}(1/16) \qquad (21f)$$

In smooth regions of the flow, the dissipative terms are of third order and do not detract from the formal second-order accuracy of the scheme. Near shocks $\nu_{i,j}$ is large and the dissipative terms become locally of first order.

Three-Dimensional Stability Limit

Applying a linear stability analysis to the inviscid form of Eqs. (19 and 20) gives the following expression for the time step.

$$\Delta t \leq \frac{CFL}{l_x |u| + l_y |v'| + l_z |w'| + \sqrt{c^2(l_x^2 + l_y^2 + l_z^2) + \Omega^2}} \qquad (22a)$$

where

$$l_x = |\xi_x| + |\eta_x| + |\zeta_x|$$

$$l_y = |\xi_y| + |\eta_y| + |\zeta_y|$$

$$l_z = |\xi_z| + |\eta_z| + |\zeta_z| \qquad (22b)$$

The Courant limit for a particular multistage scheme depends on the number of stages and the choice of coefficients α_i. See Ref. 9 for several examples.

To accelerate convergence to a steady state, we use the maximum permissible time step at each grid point so that the Courant number (CFL) is constant everywhere. The time step is calculated once based on the initial conditions. It is stored and is not updated during the calculations.

Implicit Residual Smoothing

Residual smoothing was introduced by Lerat (see, for example, Ref. 10) for use with the Lax-Wendoff scheme and was later applied to Runge-Kutta schemes by Jameson.[11] The technique involves replacing the residual calculated in Eq. (19)

with a value that has been smoothed by an implicit filter, i.e.,

$$(1 - \epsilon_\xi \delta_{\xi\xi})(1 - \epsilon_\eta \delta_{\eta\eta})(1 - \epsilon_\zeta \delta_{\zeta\zeta})\bar{R} = R \qquad (23)$$

where $\delta_{\xi\xi}$, $\delta_{\eta\eta}$, and $\delta_{\zeta\zeta}$ are standard second-difference operators and ϵ_ξ, ϵ_η, and ϵ_ζ are smoothing parameters.

Linear stability analysis has shown that the Runge-Kutta scheme with implicit residual smoothing may be made unconditionally stable if the ϵ smoothing parameters are made sufficiently large. In one dimension,

$$\epsilon \geq \frac{1}{4}\left[\left(\frac{\lambda}{\lambda^*}\right)^2 - 1\right] \qquad (24)$$

gives unconditional stability if λ^* is the Courant limit of the unsmoothed scheme, and λ is a larger operating Courant number. In three dimensions, different ϵ's may be used in each direction, and their magnitudes may often be reduced below the value given by Eq. (24).

Results

Two sets of computed results are presented for preliminary validation of the code described above. The first set of results shows the structure of a horseshoe vortex formed at the base of a cylinder standing in a turbulent boundary layer. The second set of results is for turbulent flow through an annular turbine cascade. Computed results are compared to experimental data in each case.

When a boundary layer approaches a local obstruction such as the leading edge of a turbine blade, the low-momentum fluid in the boundary layer often cannot overcome the local pressure gradient and the flow separates from the wall. In front of the obstacle the separation creates a vortex which convects around the sides of the obstacle and forms a characteristic horseshoe-shaped flow region.

Eckerle and Langston[12] have made detailed measurements of the horseshoe vortex in front of and around a cylinder of diameter D centered between the sidewalls of a wind tunnel. Test conditions included an inlet Mach umber of 0.084, $Re_D = 5.5 \times 10^5$, and an upstream turbulent boundary-layer thickness $\delta = 0.1D$. Detailed surface flow visualization and
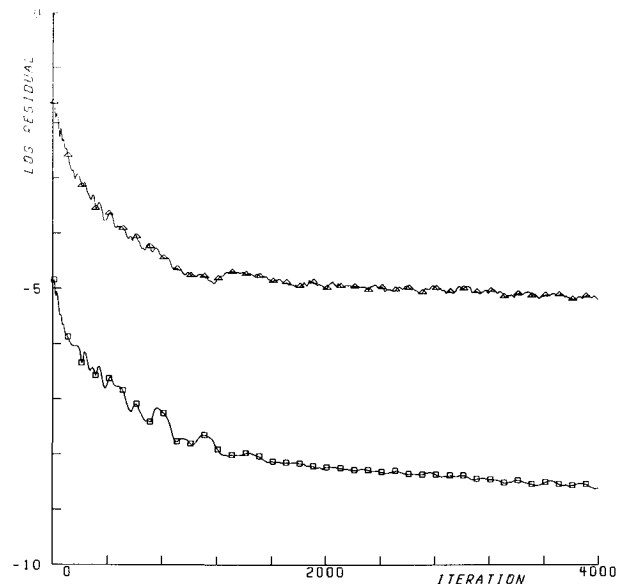
Eckerle & Langstons Horseshoe Vortex Experiment   **K = 1**
Mach   0.196   Re   538257.   Alpha   0.00   Iter   4000

Fig. 2   Convergence history for the horseshoe vortex problem.
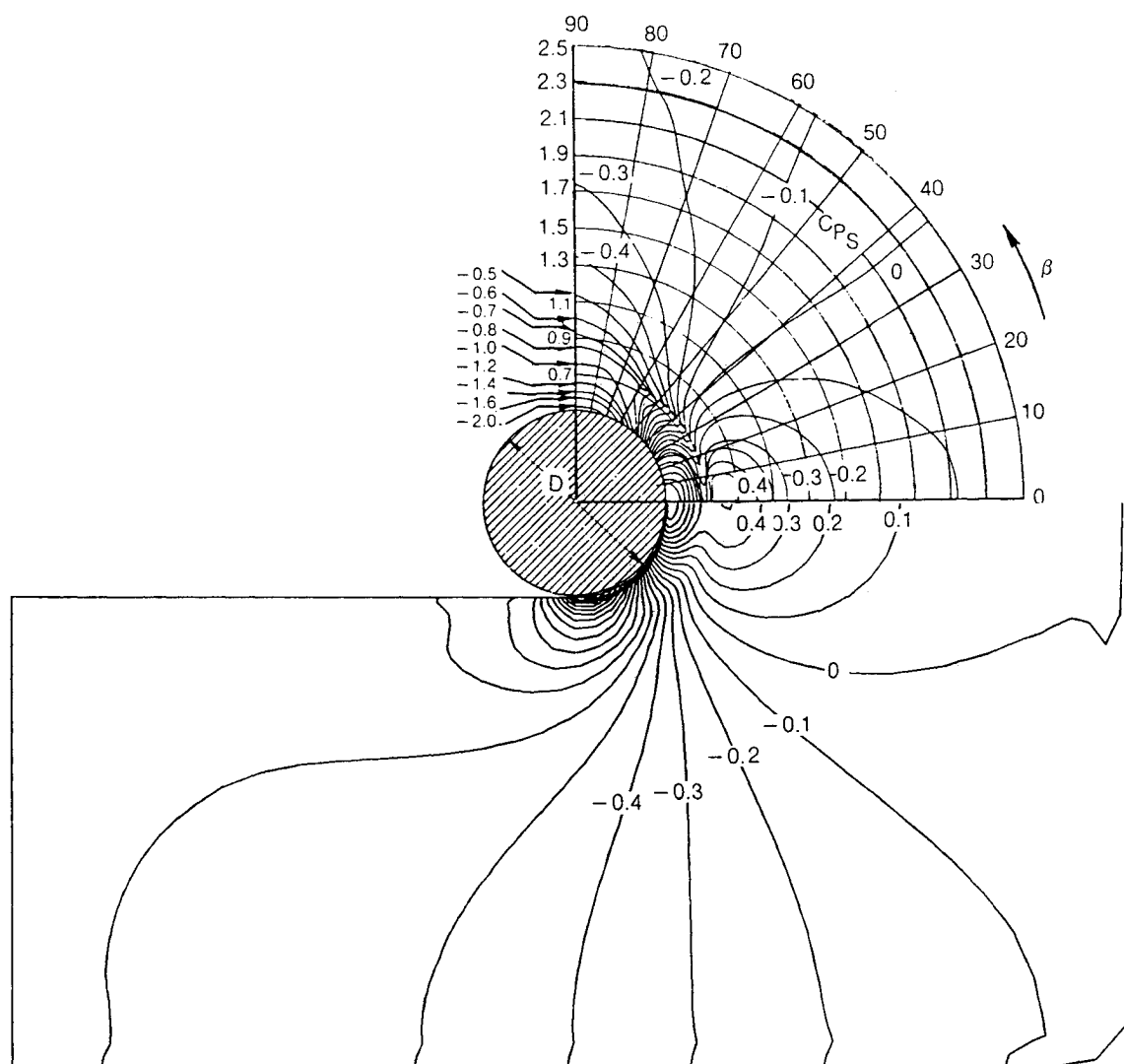
Eckerle & Langstons Horseshoe Vortex Experiment								K = 1
Mach	0.196	Re	538257.	Alpha	0.00	Iter		4000
CPS Contours		Min	− 2.000	Max	1.000	Inc		0.100

Fig. 3 Comparison of measured (top) and computed (bottom) static pressure contours on the endwall.

static pressure measurements were made, and static and total pressure measurements were taken using a five-hole probe.

Figure 1 shows the grid used to compute Eckerle and Langston's flow. The grid shown has been coarsened for clarity. The actual grid had $65 \times 49 \times 25$ points with an initial spacing at the walls $\Delta s_i = 0.0001D$. To avoid having to compute trailing-edge vortex shedding, a tail board was added from the back half of the cylinder to the exit boundary. The base grid is approximately $6D$ square and $0.5D$ high, to match the dimensions of Eckerle and Langston's wind-tunnel test section. We used a symmetry condition at midspan but computed the full symmetric flow side-to-side.

The experimental inlet Mach number of 0.084 is too low for the compressible algorithm used here, so the calculations were run with $M_{in} = 0.2$. The peak Mach number was 0.34 at the cylinder-plate junction, so the flow was essentially incompressible. The Reynolds number and inlet boundary-layer thickness were matched to the experimental data.

Even with $M_{in} = 0.2$, the four-stage Runge-Kutta scheme seemed to converge poorly, so we eventually ran the calculations using a two-stage scheme with $\alpha_i = (1.2,1)$, $CFL = 4$, and implicit residual smoothing at each stage with $\epsilon_\xi = 2$,

$\epsilon_\eta = \epsilon_\zeta = 4$. These coefficients α_i were shown in Ref. 2 to give good high-frequency smoothing. The initial convergence rate was fast, as shown in Fig. 2 by the histories of the maximum and rms residuals, but after 1000 iterations the solution showed only a tiny horseshoe vortex that did not match the data. Over the next 3000 iterations, the residuals change little, but the vortex grew and moved upstream until it stabilized at the position shown later. The total solution took 1.3 h on a Cray X-MP computer.

Figures 3 and 4 compare the calculated and experimental data on the endwall. Figure 3 shows contours of constant static pressure coefficient, defined by

$$C_{ps} = \frac{P_s - P_{sref}}{P_{0ref} - P_{sref}} \tag{25}$$

Computed contours are on the bottom and measured contours are on the top. The calculations show good agreement with the data from the symmetry plane to about 45 deg around the cylinder, where the influence of the tailboard becomes apparent. The lower part of Fig. 4 shows a flow-visualization picture made with ink dots on the endwall. It clearly shows the
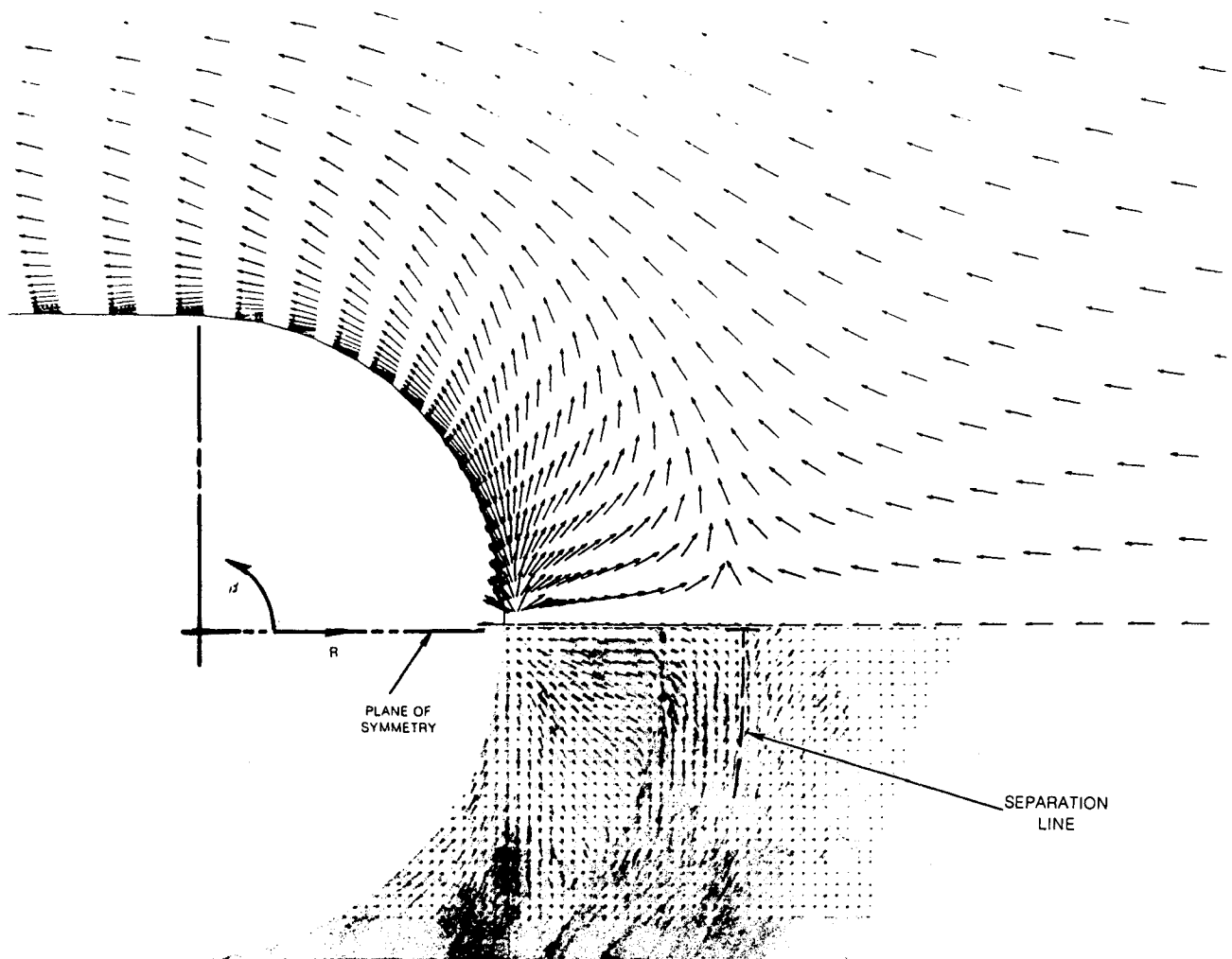
Eckerle & Langstons Horseshoe Vortex Experiment

| Mach | 0.196 | Re | 538257. | Alpha | 0.00 | Iter | 4000 |

K = 2

Fig. 4 Comparison of endwall flow visualization (bottom) and computed flow direction vectors (top) ahead of the cylinder.

separation line and reverse flow region ahead of the cylinder. The computed vector plot at the top of the figure shows close agreement with the measured separation-line location and flow directions. The vectors are one point off the endwall, and are all drawn to the same length, so they show direction only.

Figure 5 compares the static pressure coefficient distributions on the endwall along the symmetry line ahead of the cylinder. The experimental data (circles) show a general pressure rise upstream due to the cylinder blockage, but also a large dip in the pressure inside the separated region. Two vertical bars indicate substantial unsteadiness in the experimental data. Eckerle and Langston included a two-dimensional potential solution (solid line) for comparison. The computed solution (line with triangles) shows good agreement with the data ahead of the saddle point, but falls short of predicting the magnitude of the pressure dip. The discrepancy may be due to the unsteadiness in the real flow or to lack of resolution in the computed solution.

Figure 6 compares computed (bottom) and experimental (top) velocity vectors and total pressure loss coefficient contours on the symmetry plane upstream of the cylinder. The total pressure loss coefficient C_{pt} is defined by

$$C_{pt} = \frac{P_{0ref} - P_0}{P_{0ref} - P_{sref}} \qquad (26)$$

These contours show nearly horizontal boundary-layer-like flow upstream that rolls up into a vortex with a high loss core. The low-loss fluid above the boundary layer curves down the face of the cylinder and carries high-momentum fluid to the region near the cylinder-endwall junction. There is good agreement between the computed and experimental data.

The velocity vectors show how the flow rolls up to form a vortex ahead of the cylinder. Experimental velocity vectors are missing in areas where the flow angle exceeded the calibrated range of the five-hole probe. From this data, Eckerle and Langston concluded that, "The reverse flow did not roll up to form a vortex, however. The vectors clearly show that a closed vortex was not present in the plane of symmetry, though positive pitch angles in a portion of the reverse flow at $R/D = 0.72$ and $Y/D = 0.02$ may indicate the start of vortex formation. Rather than rolling up, flow passed out of the plane and proceeded tangentially around the cylinder."[12]

The computed vectors clearly show a vortex in the symmetry plane. A small counterrotating secondary vortex is also shown at the cylinder-endwall junction. The dimension of the secondary vortex is about 1.5 times the diameter of the five-hole probe, and would have been nearly impossible to detect experimentally.

The second set of results is for an annular cascade of constant profile turbine stator vanes tested experimentally by
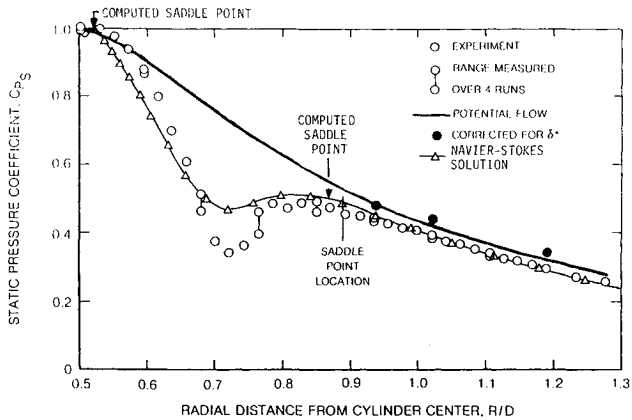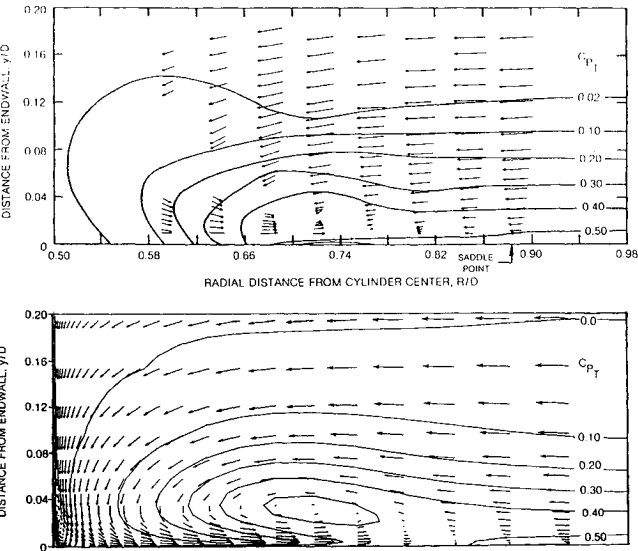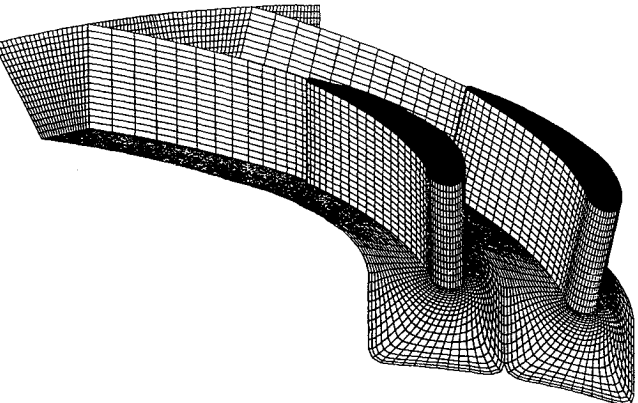
Fig. 5 Comparison of measured and computed static pressure distributions on the endwall symmetry line.

Goldman and Seasholtz[13] and Goldman and McLallin.[14] The annular ring has 36 vanes with a hub-tip radius ratio of 0.85 and a tip diameter of 508 mm. The vanes themselves are 38.10 mm high and have an axial chord of 38.23 mm. Design flow conditions are for an axial inflow with a hub-static to inlet-total pressure ratio of 0.6705. These conditions correspond to average inlet and exit Mach numbers of 0.211 and 0.665, respectively. The Reynolds number based on axial chord is 1.73×10^5.

A grid consisting of $97 \times 31 \times 33$ points with an initial

Fig. 6 Comparison of measured (top) and computed (bottom) velocity vectors and total pressure loss contours on the symmetry plane.

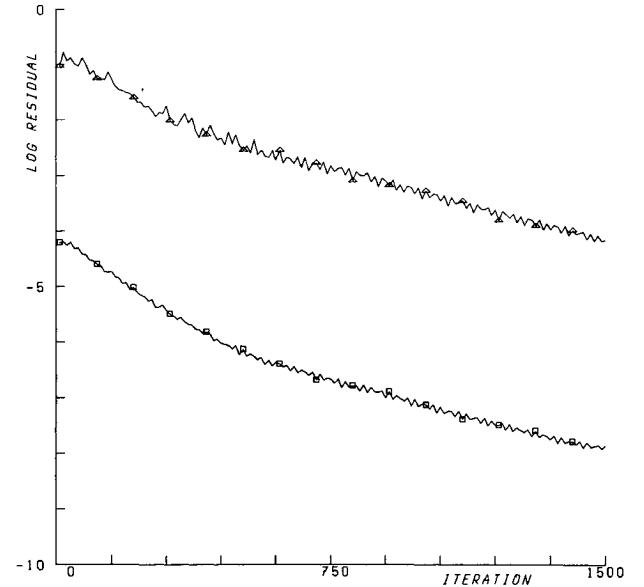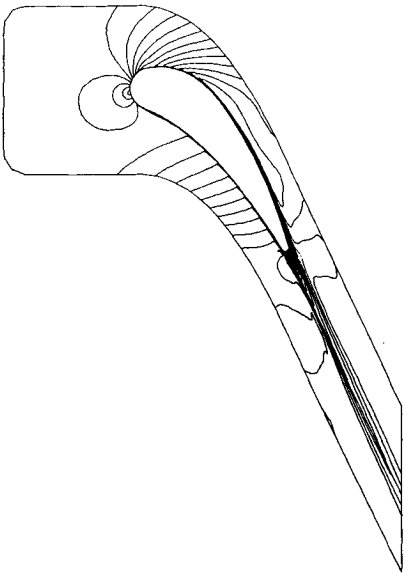| Eckerle & Langstons Horseshoe Vortex Experiment					$I = 33$
Mach	0.196	Re	538257.	Alpha	0.00	Iter	4000
CPS Contours	Min	0.000	Max	1.000	Inc	0.100

Goldmans Annular Cascade, 3-D					$K = 14$
Mach	0.212	Re	173000.	Alpha	0.00	Iter	1500

Fig. 8 Convergence history for the annular turbine cascade problem.

Goldmans Annular Cascade, 3-D					$K = 18$
Mach	0.212	Re	173000.	Alpha	0.00	Iter	1500
Mach Contours	Min	0.000	Max	0.850	Inc	0.050

Fig. 9 Mach number contours at mid span.

Goldmans Annular Cascade, 3-D					
Mach	0.212	Re	173000.	Alpha	0.00	Iter	1500

Fig. 7 Computational grid for the annular turbine cascade probelm.

spacing at the wall of 0.0002 of a blade chord was used for the flow calculations and is shown in Fig. 7.

The calculation was run with a four-stage scheme with $\alpha_i = (\frac{1}{4},\frac{1}{3},\frac{1}{2},1)$ and $CFL = 5.5$, using implicit residual smoothing after each stage with $\epsilon_\xi = \epsilon_\eta = \epsilon_\zeta = 0.75$. Convergence histories for the annular cascade calculation are shown in Fig. 8 where the log of the maximum and rms-averaged residuals have dropped approximately 3.5 orders of magnitude in 1500 iterations. The total CPU time was approximately 54 min for this calculation.
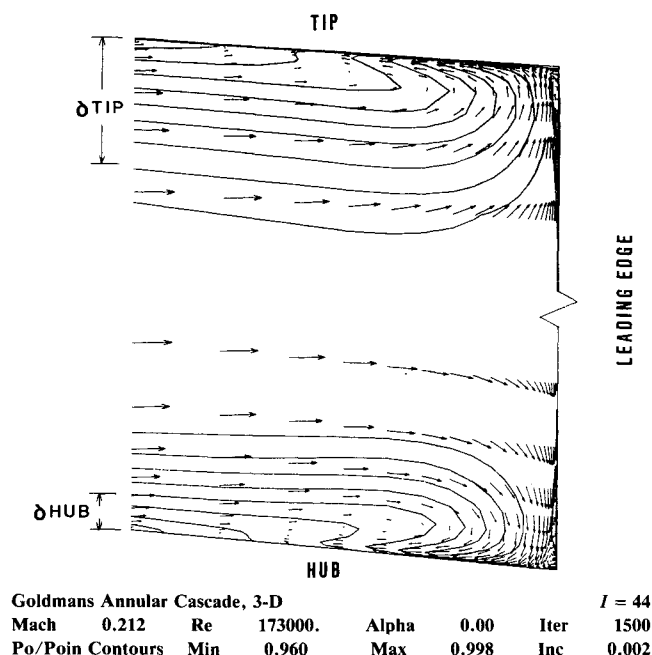
Mach number contours at midspan are shown in Fig. 9 to illustrate the blade boundary-layer and wake thicknesses. There are approximately 12 grid points across the pressure surface boundary layer.

The inlet boundary-layer thicknesses were specified as 1.9% span on the hub and 7.1% span on the tip, corresponding to the measured ata in Ref.13. In Fig. 10, velocity vectors with superimposed contours of total pressure show how these boundary layers roll up into horseshoe vortices at the leading edge of the blade. The primary vortices are considerably smaller than the inlet boundary layers, and each primary vortex has an even smaller counterrotating secondary vortex associated with it.

Figure 11 shows a comparison between the calculated surface static pressure distribution and data obtained by Goldman and Seasholtz[13] at locations of 13.3, 50.0, and 86.7% span. The calculated results agree very well with the experimental data at all spanwise locations. Although the blade section is constant from hub to tip, the increased pitch at the tip increases the loading of the tip section considerably.

Figure 12 compares calculated (top) and measured (bottom,
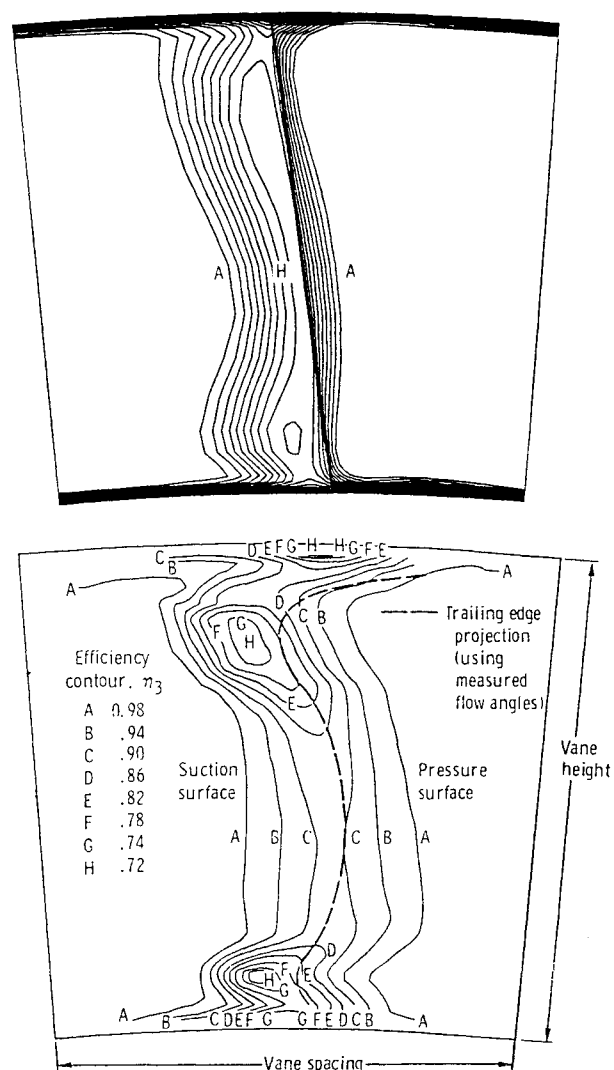
Goldmans Annular Cascade, 3-D						$I = 44$
Mach	0.212	Re	173000.	Alpha	0.00	Iter	1500
Po/Poin Contours	Min	0.960	Max	0.998	Inc	0.002

Fig. 10   Velocity vectors and total pressure contours in the endwall boundary layers near the leading edge.

Goldmans Annular Cascade, 3-D						$K = 14$
Mach	0.212	Re	173000.	Alpha	0.00	Iter	1500

Fig. 11   Comparison of measured and computed pressure distributions at three spanwise locations.

Goldmans Annular Cascade, 3-D						$K = 14$
Mach	0.212	Re	173000.	Alpha	0.00	Iter	1500
Mach Contours	Min	0.020	Max	0.980	Inc	0.040

Fig. 12   Comparisons of measured (bottom) and computed (top) efficiency contours at one-third axial chord downstream of the trailing edge.

Ref. 14) efficiency contours on a cross-channel surface located at one-third axial chord downstream of the trailing edge. The kinetic energy efficiency is theoretically independent of the axial position and is defined by the following:

$$\eta = Q_{actual}^2 / Q_{ideal}^2 \qquad (27a)$$

where

$$Q_{ideal}^2 = 2C_p T_0 \left(1 - \frac{T_{actual}}{T_0} \right) \qquad (27b)$$

and T_0 is taken as constant.

The efficiency contours clearly delineate the endwall boundary layers and wake. The computed wake is thinner than the measured wake and has higher losses (lower efficiency) at the center. The measurements also seem to show two vortical structures, presumably remnants of the leading-edge vortices, that are not seen in the computed results. However, the low measured efficiency at the center of the vortices (contour labeled H) is comparable to the efficiency along the entire span of the computed wake, indicating that the computed wake core is not sufficiently mixed out. Integrating the efficiencies over the entire area gives a total efficiency of 0.960 for the real machine and 0.923 for the calculations. The discrepancy could be due to inadequate resolution of the thick, round trailing edge, an inadequate turbulence model, or possibly to unsteady vortex shedding in the real flow. The high calculated losses seem *not* to be due to numerical dissipation. Indeed, the computed wake appears to be less dissipative than the measured wake, and the computed loss is remarkably insensitive to the artificial viscosity coefficient. Considerable work is clearly needed in the area of modeling the flows leaving blunt trailing edges commonly found on turbomachinery blades.

Concluding Remarks

A numerical analysis has been developed for three-dimensional viscous internal flows. The analysis solves the three-dimensional Navier-Stokes equations written in a general body-fitted coordinate system, including rotation about the x axis. The thin-layer approximation is made in the streamwise direction but all viscous terms are included in the cross planes. The Baldwin-Lomax eddy-viscosity model is used for turbulent flows.

An explicit multistage Runge–Kutta scheme is used to solve the finite-difference form of the flow equations. A variable time step and implicit residual smoothing are used to accelerate the convergence of the scheme. Convergence rates are slow at low Mach numbers but reasonable for typical turbomachinery applications. We hope to improve convergence rates by adding multigrid to the code.

Results showing the development of a horseshoe vortex in a turbulent boundary layer ahead of a cylinder are presented to validate the analysis. Good agreement is found between the computed results and experimental data for this case.

Results for an annular turbine cascade also show horseshoe-vortex development. Very good agreement was found between measured and computed surface pressure distributions. Computed losses were high and show the need for improved modeling of flows around blunt trailing edges commonly found in turbomachinery.

It is felt that with additional work and experience this analysis will prove to be a useful tool for investigating three-dimensional viscous flow phenomena in turbomachinery.

References

[1]Chima, R. V., "Inviscid and Viscous Flows in Cascades with an Explicit Multiple-Grid Algorithm," *AIAA Journal*, Vol. 23, Oct, 1985, pp. 1556–1563.

[2]Chima, R. V., "Explicit Multigrid Algorithm for Quasi-Three-Dimensional Viscous Flows in Turbomachinery," *Journal of Propulsion and Power*, Vol. 3, Sept.–Oct. 1987, pp. 397–405.

[3]Dawes, W. N., "A Numerical Analysis of the Three-Dimensional Viscous Flow in a Transonic Compressor Rotor and Comparison With Experiment," *Journal of Turbomachinery*, Vol. 109, Jan. 1987, pp. 83–90.

[4]Subramanian, S. V., and Bozzola, R., "Numerical Simulation of Three-Dimensional Flowfields in Turbomachinery Blade Rows Using the Compressible Navier-Stokes Equations," AIAA Paper 87-1314, June 1987.

[5]Rai, M. M., "Unsteady Three-Dimensional Navier-Stokes Simulations of Turbine Rotor-Stator Interactions," AIAA Paper 87-2058, June 1987.

[6]Baldwin, B. S., and Lomax, H., "Thin-Layer Approximation and Algebraic Model for Separated Turbulent Flows," AIAA Paper 78-257, Jan. 1978.

[7]Gessner, F. B., and Po, J. K., "A Reynolds Stress Model for Turbulent Corner Flows—Part II: Comparisons Between Theory and Experiment," *Journal of Fluids Engineering*, Vol. 98, June 1976, pp. 269–277.

[8]Sorenson, R. L., "A Computer Program to Generate Two-Dimensional Grids About Airfoils and Other Shapes by the Use of Poisson's Equation," NASA TM-81198, 1980.

[9]Jameson, A., Schmidt, W., and Turkel, E., "Numerical Solutions of the Euler Equations by Finite-Volume Methods Using Runge-Kutta Time-Stepping Schemes," AIAA Paper 81-1259, June 1981.

[10]Hollanders, H., Lerat, A., and Peyret, R., "Three-Dimensional Calculation of Transonic Viscous Flows by an Implicit Method," *AIAA Journal*, Vol. 23, Nov. 1985, pp. 1670–1678.

[11]Jameson, A., and Baker, T. J., "Solution of the Euler Equations for Complex Configurations," AIAA Paper 83-1929, July 1983.

[12]Eckerle, W. A., and Langston, L. S., "Measurements of a Turbulent Horseshoe Vortex Formed Around a Cylinder," NASA CR-3986, June 1986.

[13]Goldman, L. J., and Seasholtz, R. G., "Laser Anemometer Measurements in an Annular Cascade of Core Turbine Vanes and Comparison With Theory," NASA TP-2018, June 1982.

[14]Goldman, L. J., and McLallin, K. L., "Cold-Air Annular-Cascade Investigation of Aerodynamic Performance of Core-Engine-Cooled Turbine Vanes. I: Solid-Vane Performance and Facility Descritpion," NASA TM-X-3224, 1975.